IEEE Access
Multidisciplinary ⋮ Rapid Review ⋮ Open Access Journal

Received 31 July 2023, accepted 26 August 2023, date of publication 11 September 2023, date of current version 19 September 2023.

Digital Object Identifier 10.1109/ACCESS.2023.3313971

METHODS

Development of a 6 GHz RF-EMF Exposure System for Investigating Human Skin Temperature Responses: Characterization, Integration, and Pilot Testing

ABDELELAH ALZAHED[1], (Member, IEEE), ERIC LEMAY[1], MYKOLA ZHUK[1], GREGORY B. GAJDA[1], JAMES P. MCNAMEE[2], AND GREGORY W. MCGARR[2,3], (Member, IEEE)

[1]Non-Ionizing Radiation Physical Sciences Division, Consumer and Clinical Radiation Protection Bureau, Health Canada, Ottawa, ON K1A 1C1, Canada
[2]Non-Ionizing Radiation Health Sciences Division, Consumer and Clinical Radiation Protection Bureau, Health Canada, Ottawa, ON K1A 1C1, Canada
[3]School of Human Kinetics, Faculty of Health Sciences, University of Ottawa, Ottawa, ON K1N 6N5, Canada

Corresponding author: Gregory W. McGarr (gregory.mcgarr@hc-sc.gc.ca)

This work was supported by Health Canada and the Natural Sciences and Engineering Research Council of Canada (Grant RGPIN-2022-04276; Funding held by Gregory W. McGarr).

This work involved human subjects or animals in its research. Approval of all ethical and experimental procedures and protocols was granted by the Health Canada and Public Health Agency of Canada Research Ethics Board under Application No. REB 2021-012H, and performed in line with the Declaration of Helsinki, with the exception of prior database registration.

ABSTRACT We developed a radiofrequency electromagnetic field (RF-EMF) exposure system to investigate human skin temperature responses to localized exposures. The system was designed to project a 6 GHz RF-EMF beam with enough energy to rapidly increase peak local skin temperature on the human forearm from a baseline of 30-32°C to ∼38°C within 6 min. First, the RF-EMF exposure conditions were characterized using computer simulations to confirm that the antenna produced the desired spot size (4 cm) and resultant temperature rise in the skin. ANSYS-HFSS and Sim4Life electromagnetic and thermal simulations were performed to fully characterize the relation between electromagnetic physics and the bioheat thermal conduction problem. Next, an open-ended waveguide antenna was integrated with other hardware peripherals to comprise the full RF-EMF exposure system. Finally, human pilot testing was conducted while participants were seated comfortably with the antenna 5 cm above the skin surface on the volar (i.e. palm side) forearm. Local skin temperatures were monitored continuously with a thermal camera, which automatically identified and continuously tracked the peak skin temperature under the projected beam. Both electromagnetic and thermal data plots are presented to illustrate the bioelectromagnetic response for the exposure system. Future experimental studies using this system will examine individual and environmental factors that may influence local human skin temperature responses to RF-EMF exposures on the forearm and other body regions.

INDEX TERMS Data analysis, electromagnetic fields, electromagnetic simulations, FDTD, human exposure, radiofrequency, thermal bioheat exposure, thermal imaging, thermoregulation.

I. INTRODUCTION

Recently there has been a rapid increase in the development of fifth-generation (5G) wireless technologies operating close to the body at higher frequencies up to and including the millimeter wave range. For frequencies above 6 GHz, radiofrequency electromagnetic field (RF-EMF) exposures have the potential to produce adverse heat-related health effects such as heat-induced pain and thermal tissue injury due to an increased concentration of RF-EMF energy near the skin surface [1]. To protect the public from these adverse health effects, international bodies have provided guidance

The associate editor coordinating the review of this manuscript and approving it for publication was Sandra Costanzo.

and developed standards on safe human exposure limits, which are designed to limit the RF-EMF induced rise in tissue temperature [2], [3]. For localized RF-EMF fields in the frequency range of 100 kHz to 6 GHz, the rate of energy absorption into the tissue is described by the specific absorption rate (SAR) averaged over 10 g of tissue [2], [3]. However, at frequencies higher than 6 GHz, the absorption of the electromagnetic energy becomes more superficial [2]. As such, the absorbed power density (S_{ab}) is considered to be a more appropriate basic restriction than SAR for exposures above 6 GHz [4], [5].

In order to adequately assess potential thermal hazards from localized RF-EMF exposures at frequencies up to and including the millimeter wave range, the relation between electromagnetic radiation and the tissue temperature response has to be broadly explained. Specifically, the electromagnetic physics that define the radiating source, the medium, and field pattern, directly influence the thermal modeling accuracy and contribute to a more accurate solution to the thermal EMF interaction via Pennes' thermal bioheat equation (TBHE) [6]. Despite that, under normal conditions, it has been shown that either full or simplified versions of the bioheat equation may provide adequate insight into the thermal interaction compared to more complex numerical solutions [7], [8]. However, they still exhibit some limitations due to the random nature of the thermal interaction on human tissues. Explicitly, while some thermo-physical properties such as the thicknesses of relevant tissue layers can be easily incorporated into such models, the balance of thermal energy cannot be accurately estimated in a given volume due to local blood perfusion and tissue metabolic activity [9], [10].

To overcome the known limitations inherited in thermal modeling, there is a need for a more direct experimental testing of human tissue temperature responses to localized RF-EMF exposures, where both the exposure conditions and temperature responses are well-controlled and adequately reported [11]. This is especially true for RF-EMF exposures at frequencies at and above 6 GHz, where the majority of energy is concentrated in superficial tissues such as the skin and cornea [1]. With that in mind, the objective of the current work was to provide a comprehensive description of the development, characterization, and experimental validation of a straightforward system for tracking skin temperature responses to localized 6 GHz RF-EMF exposures in human participants. The system was designed around a dual port open-ended square waveguide antenna capable of generating an RF-EMF SAR spot, where the SAR spot is defined as the area on the surface on which the SAR is deposited, with enough energy to rapidly increase peak local skin temperature on the human forearm from a baseline of 30-32°C to ~38°C within 6 min. This time period is sufficient to generate a rapid and robust temperature rise in the skin while avoiding heat-related pain and thermal tissue injury. Future studies using this system can be used to improve upon existing theoretical thermal models, supporting the assessment of localized RF-EMF exposures from sources that are in close proximity to the body.

The manuscript is organized as follows. In Sec. I, we start with the design rationale of the waveguide itself and how it can be utilized to assess human skin temperature responses during localized RF-EMF exposure experiments. In Sec. II we present the thermal modeling process via the bioheat thermal equation. In Sec. III, we outline the design and principle of the open-ended waveguide in terms of its operating frequency, physical dimensions, and field plots. A simulation of the proposed design was carried out using Sim4Life EM-software to investigate and compare the EM characteristics of the device in isolation and in the presence of a human tissue model. In Sec. IV, we move to the system-level design and the implementation of the entire RF-EMF bioheat exposure system. We start by defining the system peripherals, connections, and data processing and end with a description of the thermal camera setup. In Sec. V, we describe the simulation setup in Sim4Life that was used to predict the local tissue temperature response to the RF-EMF exposure. In Sec. VI, we analyze the thermal data captured by the camera from a human participant in which we examine the governing relationship between the RF-EMF spot size and the peak skin temperature rise where the spot size is the size or diameter of the half-power SAR isoline. The skin temperature response is analyzed using open-source scripts developed in Python to estimate the resulting SAR and S_{ab}. Finally, in Sec. VII, we conclude by outlining future applications of the proposed bioheat exposure system.

II. THERMAL MODELLING

The multi-physics solvers (Ansys-HFSS [12] and Sim4Life [13]) used in this project are capable of generating solutions of the thermal bioheat equation (TBHE) directly from a description of the source and target tissue. However, to be useful to the wider thermal modeling community, it is helpful to present the electromagnetic characteristics of the source in terms of approximate parameters that are used in thermal modeling. For this purpose, the terminology and definitions presented in [14] will be used.

The input energy term in the TBHE is the SAR and its distribution. For simplicity, the 3D SAR distribution can be decomposed into 1) an axial distribution, where the SAR versus depth (i.e. z coordinate) in a tissue composed of planar layers, is described and 2) a transverse distribution. The latter is assumed to be cylindrically symmetric (a function of the radial dimension, r) and is assumed to have a Gaussian shape. The resulting 2D (cylindrically-symmetric) SAR distribution can be written as:

$$SAR(r, z) = SAR(z) \cdot exp(-r/w_2) \tag{1}$$

where w_2 is the Gaussian variance.

A convenient parameter to work with when describing the transverse distribution is the width of the half-power isoline, termed the full width at half maximum (FWHM), from which

the root of the variance is found to be $w = 0.601$ FWHM. For convenience throughout the remainder of this work, the FWHM will also be referred to as the ''spot size'' with the term ''spot'' referring to the axial transverse SAR distribution. For practical sources, the transverse distribution width is not symmetric i.e. the FWHM along the two transverse coordinate axes x and y are not usually equal. In the case that they are significantly different, it has been shown [Gajda, private communication] that the temperature rise estimate is correlated to the geometric mean of the FWHM along the x- and y-axis (denoted as FWHMx and FWHMy, respectively). Thus, the FWHM used in the approximate modeling is given by:

$$\text{FWHM} = (\text{FWHMx} \times \text{FWHMy})^{0.5} \tag{2}$$

The axial distribution of the SAR, SAR(z), can be extracted from the EM solution of the source projecting its beam onto the surface of the multi-layer, planar tissue. For heterogeneous tissues, SAR(z) is in general, non-monotonic whose relative amplitudes in each layer are determined by the multiple reflections occurring between layers. In cases where the source is sufficiently removed from the tissue, the axial distribution will resemble that which would be produced by a plane wave. Under these conditions, the modeling procedure can be simplified by use of a straightforward plane wave propagation model to compute the relative amplitudes in the various tissue layers. Once this has been completed, it only remains to match the SAR at the surface, SAR(0), to the experimentally determined value in order to fully describe the experimental axial SAR distribution. Once the axial SAR distribution has been found and the FWHM either measured or computed, simplified, or detailed solutions of the TBHE can be carried out using assumed values of thermal conductivity and blood perfusion rate in an attempt to ''curve-fit'' the measured tissue temperature response. This would be difficult to perform using the built-in thermal solvers in Ansys-HFSS and Sim4Life owing to the long computation times.

III. RADIATING SOURCE: PRINCIPLE AND DESIGN

Over the past few decades, open-ended waveguides have proven to be useful in a variety of microwave and millimeter wave assessment applications. They are now extensively used in many non-destructive testing and evaluation applications, including measurement and characterization of dielectric material properties, determining the thickness of dielectric slabs [15], [16], and in some medical applications [17]. Originally, waveguides were commonly used as transmission lines to carry EM signals from one end to the other with low losses and almost no EM leakage [18]. They are shaped and fabricated according to the desired operating frequency, allowing propagation above, and attenuation below, the cut-off frequency, respectively. The main advantage resides in the ability of the waveguide to block external radio waves from interfering with the guided waves in the direction of propagation and vice-versa due to the conducting walls. In addition, the waveguide has the ability to project a highly directional beam along its axis. Overall, open-ended waveguide antennas are useful in a variety of applications where precise control of the electromagnetic wave is desired. In the current bio-heat experiment, we focused on frequencies above or equal to 6 GHz with the main SAR spot applied to a small area of a participant and with the waveguide placed in very close proximity to the skin surface. As a result, the waveguide interacts (couples) with the participant such that radio waves bounce back from the tissue section and couple back with the waveguide EM waves. Typically, the reflection coefficient at the aperture of the waveguide is directly related to the operating frequency, as well as the dielectric and geometric properties of the medium. Therefore, in order to calculate the isolation coefficient, the relationship describing the mutual interaction of the fields launched from the waveguide aperture into the medium under test must be determined. The latter will be examined in this work by investigating the waveguide port isolation using EM simulations, and in the presence of a 3-layer human tissue model.

The following sub-sections provide details on the waveguide design, port excitation/response, and field patterns. They are organized as follows. The first sub-section outlines the simulated design of the 2-port waveguide antenna by showing the dimensions, frequency, and port locations. The second sub-section focuses on the EM results in two scenarios by observing the self and mutual interactions of the excitation ports and the radiated fields. The third sub-section provides a comparison between the measured and simulated port responses in a free-space unperturbed scenario.

A. WAVEGUIDE DESIGN

A square waveguide was selected as shown in Fig. (1) to serve as the RF-EMF source due to its simple design and construction, as well as its ability to project a roughly circular beam onto the skin surface that tapers at its edges in a well-defined way. The proposed waveguide consisted of two port excitation probes mounted at 90-degree separation) in order to support two propagating modes. Due to manufacturing tolerances, the local fields in the vicinity of an excitation probe will excite the orthogonal mode (i.e. a probe aligned along the y-axis is meant to excite the TE_{10} mode). However, it will also excite a relatively weak TE_{01} mode (the first and second integers in the mode numbering format refers to the number of half-periods in the x and y directions, respectively). This is due to the local fringing fields around the probe that have components in both transverse directions. In a traditional rectangular waveguide, the orthogonal mode would still be excited but would then be attenuated due to propagation below cut-off. Namely, in the field reflected from the aperture and travelling toward the connectors, the fundamental polarization will be totally accepted by the principal port, and the cross-polarized component by the orthogonal port. Once the mode is conducted into the respective port, it is absorbed by the generator (the principal port) or by the matched load (the orthogonal port). This eliminates possible resonant phenomena in the waveguide involving either the

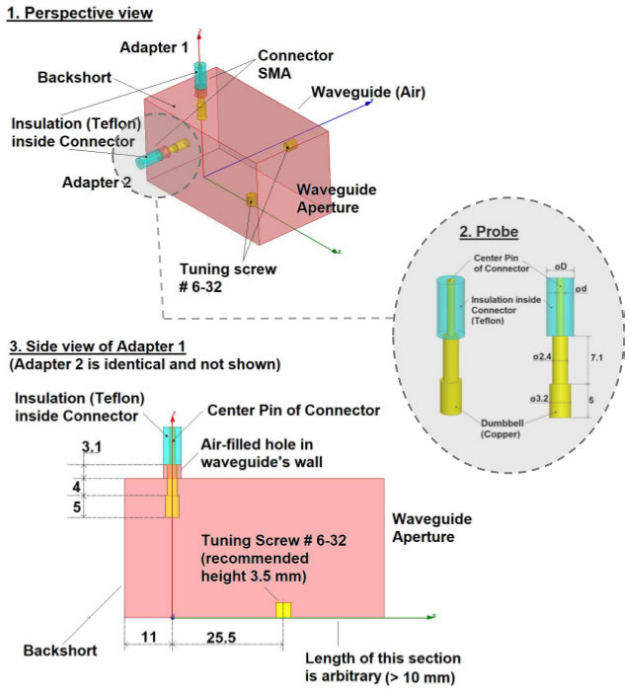

FIGURE 1. An open-ended square waveguide antenna designed in ANSYS-HFSS to operate at 6.0 GHz. 1) Perspective view of 32 × 32 mm^2 inner dimension square waveguide, 2) SMA excitation with dumbbell outside-diameter (oD) of 4.11 *mm* and inside-diameter (od) of 1.27 *mm*, and 3) side view of the waveguide applicator (shaded area). All dimensions are given in *mm*.

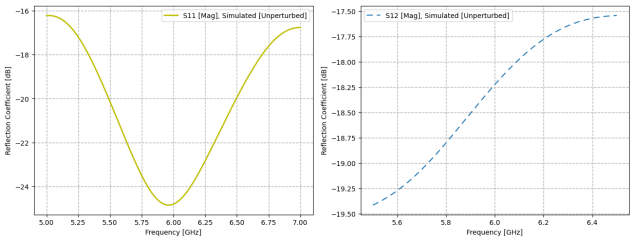

(a) S_{11} (b) S_{12}

FIGURE 2. The simulated reflection coefficient of the excitation port (S_{11}) and isolation (S_{12}) to the second port of the waveguide adapter.

fundamental polarization or the cross-polarization. In this paper, the excitation is made to one port while loading the other.

The initial EM simulation of the waveguide port was carried out using ANSYS-HFSS where the return loss is given in Fig. (2). In order to achieve a better return loss around the resonance, the waveguide length was extended to 85*mm* and a return loss of more than 30 dB was achieved as will be shown in the following section.

The Sim4Life 3D electromagnetic solver [13] was used to simulate the open-ended square waveguide antenna of the extended length, and to optimize the location of the coax-to-waveguide adapter, and the dimensions of the excitation probes. The electromagnetic simulation also ensured

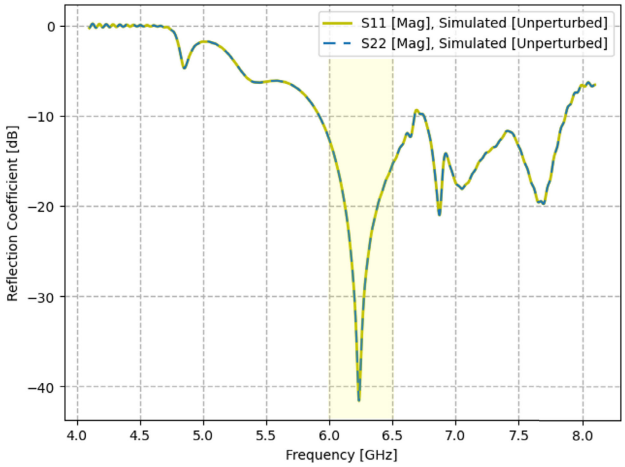

FIGURE 3. The reflection coefficient (S_{11}, S_{22}) of the unperturbed square waveguide. Port responses are identical due to the imposed symmetry.

that no other modes co-existed with the fundamental operating mode. The waveguide was constructed of commonly available aluminum square tubes and optimized to launch an RF wave at 6.1 GHz with exterior dimensions of 32 × 32 mm^2, and a wall thickness of 3.048 *mm*. The waveguide was milled, drilled, and assembled in-house. Furthermore, an aluminum back plate cut from solid aluminum stock was trimmed and press-fitted into the waveguide in order to form the back-short. The waveguide length between excitation and back-short is extended by the thickness of the aluminum plate (the back-short). Nevertheless, the excitation probe is soldered to the center pin of a bulkhead SMA coax connector, and the latter is mounted to the aluminum waveguide with holding screws.

B. ELECTROMAGNETIC RESULTS

A full electromagnetic simulation was performed for two possible scenarios where the first scenario described the waveguide in isolation (unperturbed) and the second included a 3-layer tissue model (perturbed). The simulation provided details on the port matching, isolation between orthogonal ports, aperture mode, and power density. Here, the aim was to study the impact of the 3-layer tissue on the waveguide ports' response, as discussed in the following sub-sections.

1) SCENARIO I: UNPERTURBED SIMULATION

The Sim4Life electromagnetic solver was used in the subsequent simulations. To reduce the computational complexity for this scenario, the waveguide was modeled as a perfect electric conductor (PEC) and a Teflon dielectric of a relative permittivity of 2.08 to model the SMA dielectric portion. To verify the waveguide functionality, we investigated the self-interaction coefficient (S_{11}) on each port, which is depicted in Fig. (3). A return loss of 38 dB was observed over a 10-dB bandwidth of about 500 MHz at the center frequency, for both ports.

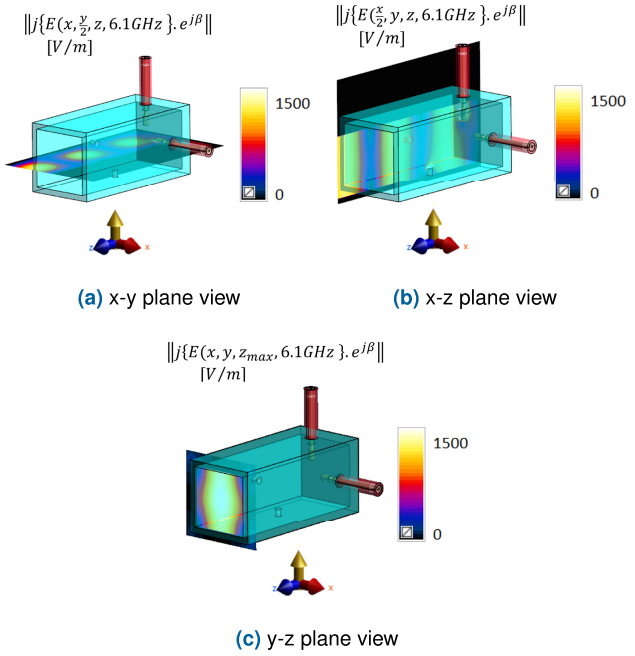

FIGURE 4. 2D view of the imaginary field component of the E-field in a 2D slice view inside the square waveguide at the operating frequency $f_0 = 6.1GHz$. The plot shows the field intensity in (a) x-y plane, (b) x-z plane, and (c) y-z plane.

In unperturbed conditions, the operating mode can be viewed by investigating the fields inside the waveguide as shown in Fig. (4). Using a single port excitation, the fields correspond to the TE_{10} mode where the imaginary component of the E-field occurs in the x- and y- directions. For 1 Watt input power, the E-field has a maximum intensity of $1500V/m$ in the observed planes.

2) SCENARIO II: PERTURBED SIMULATION

The second scenario of the experiment involved adding the 3-layer local human tissue model, skin: 1mm, SAT: 6mm, and Muscle: 60mm, to the waveguide simulation environment in order to study the EMF perturbations on the waveguide section and to observe the RF-EMF exposure parameters (SAR and S_{ab}. The block was placed at a distance of 5 cm (or 1 free-space wavelength) from the waveguide aperture and the tissue surface was extended to almost four times the size of the aperture area. The exposure level was measured by observing the SAR and S_{ab} on the skin layer. The maximum intensity of 274 W/m^2 (power density), and 91.4 W/kg (SAR) were computed at the center of the exposed area on the surface as shown in Fig. (5) and (6), respectively. The power density was formulated using the transverse E- and H-fields inside the skin and calculated at different frequencies in the operating band.

Moreover, the SAR intensity and shape was observed at different frequencies as shown in Fig. (6) where the SAR shape gradually evolved from an elliptical shape to a more circular symmetric shape as the frequency was increased. The previous observation is expected to occur between a large sample of participants where a slight deviation of frequency can influence the spot size. At the operating frequency, the axial SAR distribution in the center of the SAR spot in Fig. (7) showed a maximum SAR of 91.4 W/kg on the skin surface and steadily changed as the wave penetrated deeper into the tissue layers. The 3-layer tissues are highlighted as indicated in the figure where the order of the layers from left to right is: skin, subcutaneous adipose tissue (SAT), and muscle. A comparison to the plane wave propagation model (PWPM) [19] was made using analytical modeling and plotted in Fig (7).

In summary, the plots in Figs. (5) and (6) highlight the characterization of the electromagnetic wave when it impinges on the 3-layer tissue and the skin surface, yet it does not provide details on how to determine differences between the unperturbed and perturbed cases with respect to the fields inside the waveguide. Therefore, the EM effect of the 3-layer tissue model on the RF device was characterized by inspecting the isolation between the ports in the two cases (unperturbed and perturbed). Fig. (8) and Fig. (9) show the S_{11} and S_{12} in the two scenarios, where the 3-layer tissue model imposed an isolation factor of more than 5 dB at 6.1 GHz to the excitation port in comparison to the unperturbed case. Moreover, a zero isolation difference between the two cases was observed at about 6.2 GHz and 5 cm distance. Further, the self-interaction S_{11} coefficient plot has almost 20 dB degradation at the resonance caused by the tissue while other resonances have been excited at 5.5 and 7 GHz. In the perturbed simulation, the S_{11} and S_{12} values at each frequency were: -5.3 dB, -7.5 dB at 6 GHz, -10.3 dB, -4.2 dB at 6.1 GHz, and -15 dB, -7.4 dB at 6.2 GHz, respectively.

After a successful simulation, waveguide performance was viewed by inspecting the RF-EMF response on the tissue surface. The simulated 3D temperature and SAR spot, as shown in Fig. (9), represents the field intensity distribution impinging on the skin surface in both horizontal and vertical directions. Thus, the normalized field intensity and spot size were reported for both the temperature and SAR as indicated in Table (1). In addition, the reported spot size was calculated at the highest intensity point and at the FWHM level (i.e., at 50% of a brief RF exposure). Also, both horizontal and vertical data, depicted in the figures as Hor and Ver, respectively, were fitted to a Gaussian function that carried the signature of the spot size, and intensity [20], and is represented as follows,

$$y = A \cdot exp\left(-\frac{x - x_0}{B}\right)^2, \tag{3}$$

where A, B, and x_0 correspond to the peak power, normalized dimension, and Gaussian variance, respectively. However, the actual dimension was estimated by finding the inverse square of the normalized dimensions, A and B.

In order to calculate the parameters in Table (1), we examined the 2D line-profile (projected spot shape in a 2D plane) and SAR data. First, the spot size was calculated by estimating the horizontal and vertical dimensions of the Gaussian fit function in Eq. (6). That is, the Gaussian fit was applied to

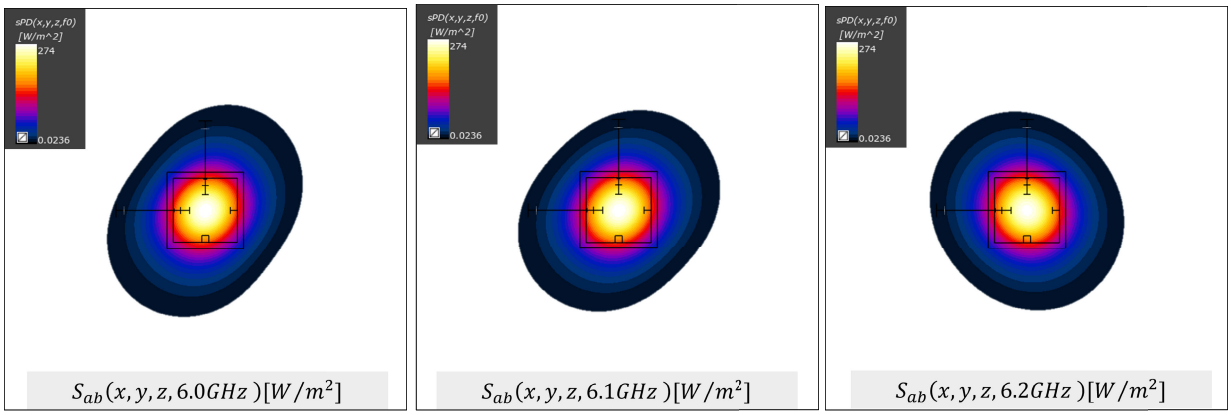

(a) S_{ab} at 6.0 GHz (b) S_{ab} at 6.1 GHz (c) S_{ab} at 6.2 GHz

FIGURE 5. 2D slice view of the absorbed power density (S_{ab}) under the skin surface at different operating frequencies.

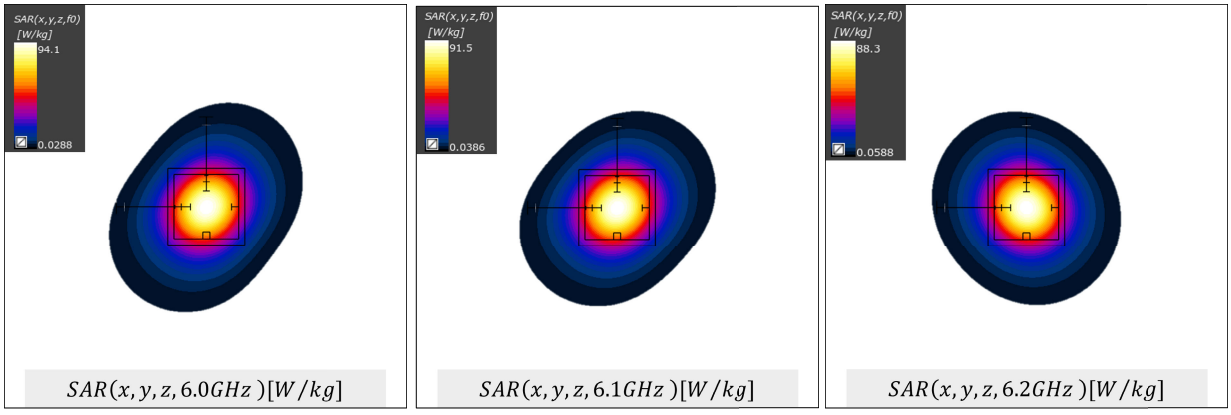

(a) SAR at 6.0 GHz (b) SAR at 6.1 GHz (c) SAR at 6.2 GHz

FIGURE 6. 2D slice view of the SAR distribution of the square waveguide on a 3-layer tissue at different operating frequencies.

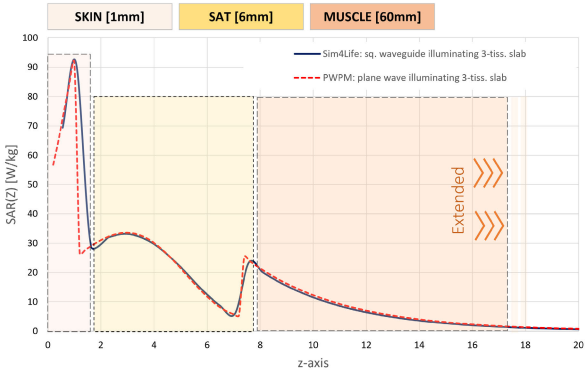

FIGURE 7. Axial SAR distribution along the z-axis at 6.1GHz operating frequency, comparing the Sim4Life SAR simulation (solid line) and the PWPM model (dashed line).

either the temperature or SAR profiles. Using the temperature and SAR data, the S_{ab} was calculated using the spot size and the RF input power, while the SAR was extracted by selecting a short time interval from the temperature data at the beginning of the experiment and by applying the following discrete differential formula.

$$\text{SAR} = C \cdot \frac{\Delta T}{\Delta t} \tag{4}$$

TABLE 1. Simulated 3D Temperature Data (40 seconds RF exposure) and SAR profile.

Parameter		Temp. Data	SAR Profile
FWHM x-Hor	$[mm]$	33	33
FWHM y-Ver	$[mm]$	33	33
S_{ab}	$[W/m^2]$	364.7	274
SAR	$[W/kg]$	191.82	91.4

where C is a heat capacity constant, T is the temperature, and t is the time in seconds.

Above 6 GHz operating frequency, the relationship between the half power beam diameter (HPBD) and FWHM is formulated as in Eq. (5) where they represent the spatial average of the external power density, and the temperature rise over a relatively long time window, respectively. The ratio was examined within the framework of the proposed RF-EMF exposure system [14].

$$\text{FWHM} = \text{HPBD} \cdot k, \tag{5}$$

where the FWHM and HPBD correspond to a specific antenna type with the HPBD equal to or larger than the FWHM, where the latter is strongly related to the normal component of the Poynting vector [21], and k is a constant

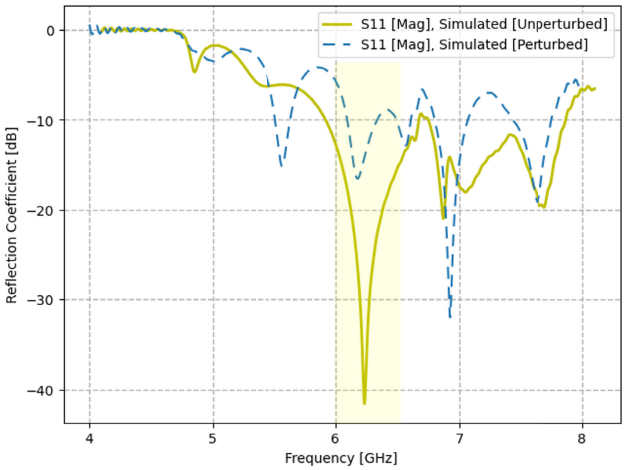

(a) S_{11}

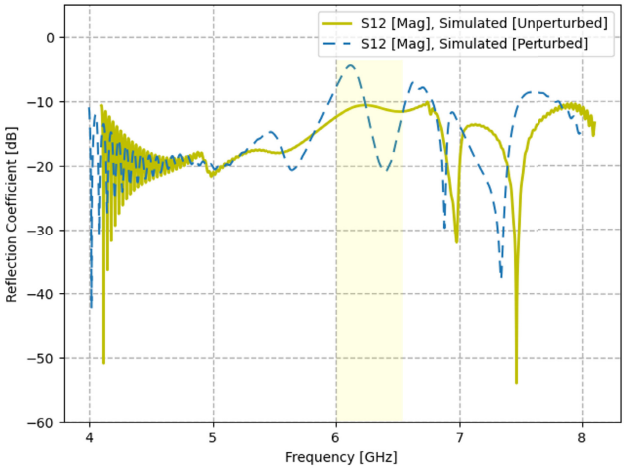

(b) S_{12}

FIGURE 8. A comparison plot of the reflection coefficients S_{11} and S_{12} between the unperturbed and perturbed simulations in a frequency range between 4-8 GHz.

between 0 and 1 that corresponds to the absolute ratio between the two parameters. As a result, the average FWHM can be expressed for the temperature and SAR data profiles as 40 *mm*, and 32.25 *mm*, respectively.

C. MEASUREMENT AND SIMULATION

In accordance with the previous simulated data, a validation of the port response was conducted by comparing the results to the measured data. More specifically, the self and isolation coefficients of the excitation port of the constructed square waveguide was evaluated using a Network Analyzer (Agilent E5071C), to ensure the waveguide had the optimal performance to launch RF waves in the frequency band of interest. The tuning screws were adjusted in order to achieve a return loss on both ports in the order of -30 dB. A comparison of the reflection coefficients of the measured and simulated data are shown in Fig. (10).[1] The testing was conducted in the

[1]The frequency offset between the measured and simulated data is due to fabrication tolerance and was calculated to be less than 50MHz off the resonance.

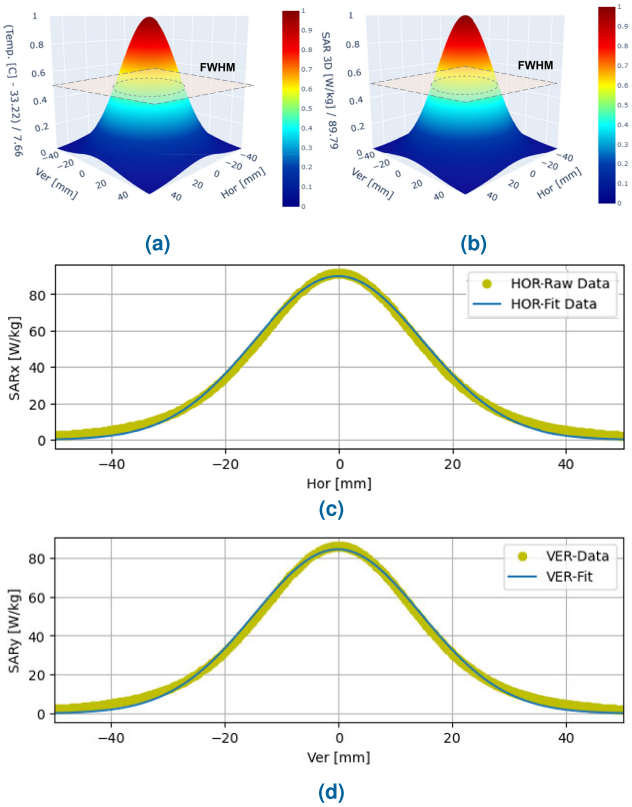

FIGURE 9. 3D representation of (a) temperature and (b) SAR (projected spot size). The 2D raw and fitted data representation of the SAR are shown for (c) horizontal and (d) vertical lines.

same environmentally controlled laboratory where the human experiments were performed.

IV. ELECTROMAGNETIC BIOHEAT EXPOSURE SYSTEM

As depicted in Fig. (11), the electromagnetic bioheat exposure system consisted of an RF signal generator, a power amplifier, a dual directional coupler, power sensors, a square waveguide, a thermal camera, and a data processing unit. Each hardware module required to perform the desired experiment is discussed in this section.

The RF signal generator (Gigatronics 2520B) [22] was used to launch the RF signal to the power amplifier module by setting up the signal type, frequency, power, and magnitude offset. The power amplifier (Microwave Amps Ltd. AM43-5.8-6.4-47-47) [23] was used to amplify the RF input power by 47dB, to achieve an output power of about 44dBm, to optimize for the exposure dose and duration, and to achieve a robust peak local skin temperature without causing heat-related pain or thermal tissue injury [10]. The power line-up in the RF signal chain was measured using multiple power sensors (NRP Z11, Rhode & Schwarz) that are connected to a power meter (NRP, Rhode & Schwarz). The power meter [24] provided details on the output power from the amplifier and the waveguide port (as described in Sec. III). That is, the power was continuously monitored during the experiment to avoid any rapid overshoots or sudden power losses. Finally, the directional coupler served as

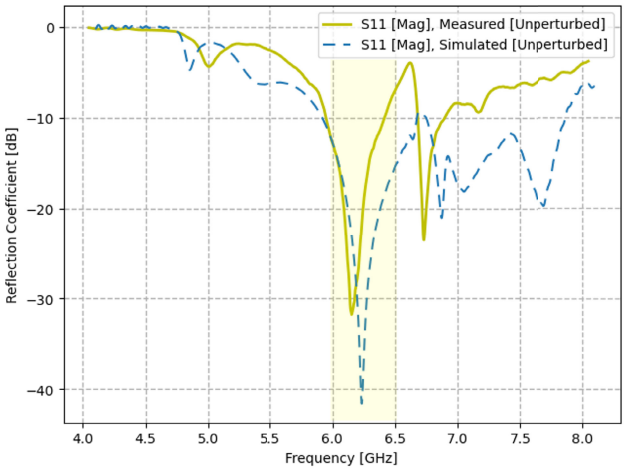

(a) S_{11}

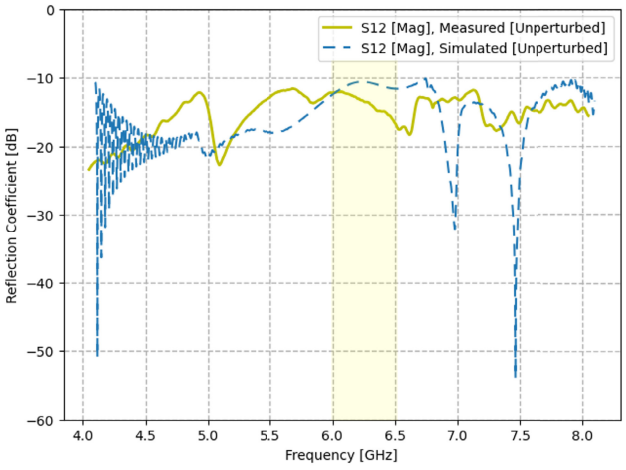

(b) S_{12}

FIGURE 10. A comparison between the simulated and measured reflection coefficients in dB of the proposed square waveguide. (a) self-interaction (S_{11}), (b) isolation (S_{12}).

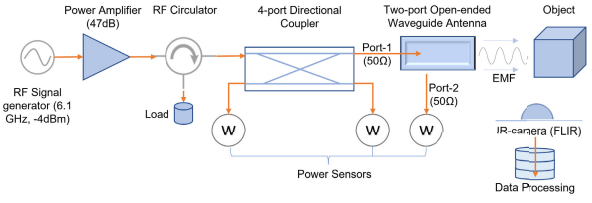

FIGURE 11. Bioheat exposure system block diagram. The diagram provides a high-level description of the system blocks and hierarchy. The system comprises an RF signal generator, RF peripherals, a waveguide antenna, a thermal camera and a data processing module.

a multi-port power routing switch, allowing for power measurements at different points under normal operating settings.

A high-definition thermal camera (FLIR A700) [25] was mounted close to the waveguide aperture at a 45-degree angle. The waveguide aperture was positioned at one-wavelength distance (5 cm) from the participant while the camera was almost two-wavelengths from the participant. The camera was capable of providing an infrared resolution of 640 × 480 pixels, a detector pitch of 12 μm, and a frame rate of 30 Hz. The measurement accuracy was about ± 2°C

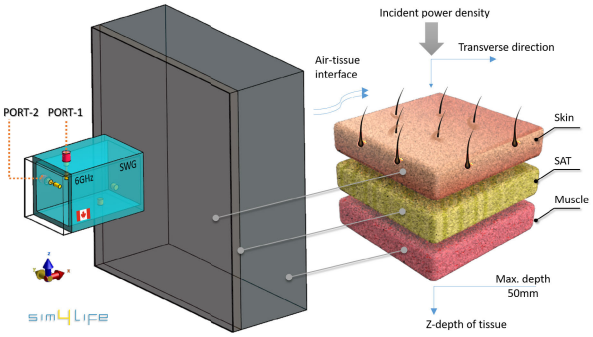

FIGURE 12. 3D CAD model using Sim4life. The model includes a 3-layer tissue (skin (1 *mm*), SAT (6 *mm*), and muscle (60 *mm*)). The square waveguide (SWG) is placed at a 5 cm distance from the skin surface.

of reading for ambient temperature between 15°C to 35°C. Absolute temperature was calibrated against an external black body calibrator (BB702, Omega Sensing Solutions ULC, QC, Canada). The camera was controlled using computer software that displayed temporal-temperature data and line-profile information. The line-profile data describe the spatial temperature distribution on the exposed region of interest (ROI). Specifically, the ROI had a default rectangular shape with dimensions of 3.4 × 4.3 cm^2. After a successful measurement, the final data were exported in tabular format for post-processing and analysis purposes. The analysis section was performed using open-source Python scripts.

V. SIMULATION SETUP

The EMF effect of the square waveguide on a 3-layer tissue model was studied using Sim4Life simulation software. The tissue model in Fig. (12) consisted of 1 *mm* of skin, 6 *mm* of subcutaneous adipose tissue, and 60 *mm* of muscle. The tissue parameters used in the simulation were taken from [26]. The 3-layer tissue is placed 5 cm (one wavelength) from the aperture of the square waveguide in order to have the waveguide in close proximity to the exposed area without blocking the thermal camera. As mentioned earlier, the power density along with the SAR were used as metrics to evaluate the RF-EMF exposure at the outer surface of the skin layer. As such, the latter was estimated from the line-profile and temporal-temperature data collected by the thermal camera.

VI. HUMAN EXPOSURE ASSESSMENT AND DATA ANALYSIS

The human RF-EMF exposure testing was approved by the Health Canada and Public Health Agency of Canada Research Ethics Board (REB 2021-012H). Written and informed consent was obtained prior to participation. One healthy, habitually active male (age = 24 years, height = 183 cm, body mass = 100 kg) completed the experiment. The exposure assessment was conducted in an environmentally controlled room with an air temperature of 23°C and relative humidity of 32%. The participant was seated comfortably with the right arm extended in front of the body in the supine position so that the volar forearm (i.e. palm side) was

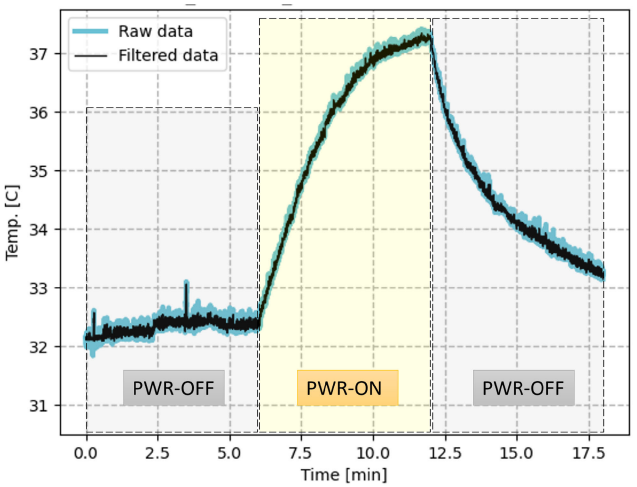

FIGURE 13. Peak skin temperature profile from one participant. The plot shows the temperature profile from the underside of the forearm before, during, and after exposure to a 6.1 GHz EM wave. The plot shows the two phases of the data processing results (1, and 2). The first layer shows the raw data (high noise), and the second layer shows the final version of the filtered data (low noise).

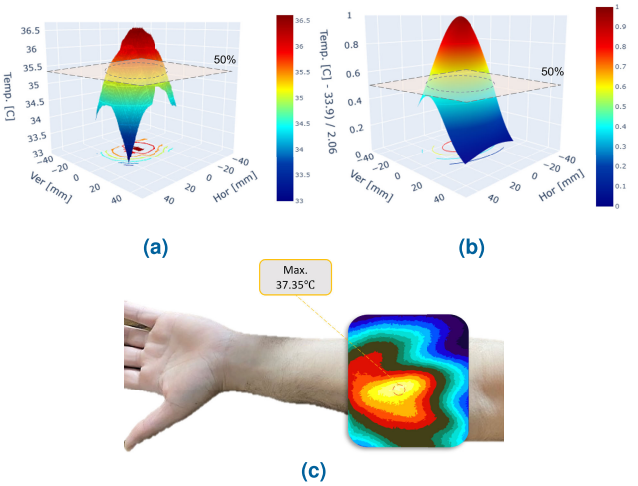

FIGURE 14. 3D representation of the line-profile data. The plots show the 3D temperature profile shape (a) raw, and (b) filtered. (c) Thermal response of the RF-EMF exposure on the underside of a forearm of the participant. The measured area is acquired using the FLIR camera and by observing the peak temperature after a 6 min exposure.

exposed to the RF-EMF source. The waveguide antenna was placed 5 cm above the skin surface over the medial third of the forearm. Further, RF absorbing sheets were placed on the platform supporting the arm to suppress scattered fields. Local skin temperatures in the exposed area were monitored continuously with the thermal camera, which automatically identified and continuously tracked the peak skin temperature under the RF-EMF spot.

The assessment of the bioheat thermal experiment was carried out by analyzing the temporal temperature data of the examined section of human tissue (e.g. volar forearm). The data consists of three parts (i.e., three time domain intervals), the pre-exposure baseline (RF power-off), the rise of peak skin temperature during the RF-EMF exposure (RF power-on), and the fall in peak skin temperature post-exposure (RF power-off), in which the transition defines the power on and off switching of the radiating source. Thus, in order to observe the hot spot size, line-profile data plots were used at the peak observed skin temperature of the temporal data. Ideally, the profile (the hot spot) follows a pattern of a Gaussian shape in the 2D plane comprising the data. Both of the resulting data, i.e., temporal and line-profile, provide information on the power density, SAR, and temperature variation. In Fig. (13), the temporal temperature profile is shown for a six-minute exposure of a 6.1 GHz EMF on the underside of the forearm.

The raw data were analyzed into two components: time-windowed and filtered data. The windowing process discarded intervals/points in which rapid changes or spikes were observed before or after the test interval. The filtered data were the analytical de-noising and smoothing process that minimized small oscillations embedded in the test data. The comparison between the two stages is presented in Fig. (13). In order to study the S_{ab} of the exposure system, we investigated the line-profile data at the observed peak temperature. In Fig. (14) and (15), the 3D and 2D spot plots are shown at different data processing stages.

The line-profile data were captured at a peak local skin temperature of ∼37.35°C after 6 min of continuous, steady-state exposure. In order to visualize the peak skin temperature on the FLIR application interface (API), the line-profile ROI was manually adjusted to an expected/estimated spot on the display of the thermal camera such that the peak temperature was observed close to the center of the profile. As shown in Fig. (14), the 3D spot shape matches a Gaussian distribution across the 2D plane in both the horizontal and vertical directions. Note that the horizontal and vertical lines define the x-axis and y-axis, respectively. The data are mathematically expressed using the Gaussian function in Eq. (6). The previous process was performed to obtain an analytical formulation of the spot size, FWHM, and HPBD [20].

The resulting SAR, S_{ab}, and temperature profile were fitted to the Gaussian function in Eq. (6) and are shown in Fig. (16). The definitions of HPBD and FWHM of the skin SAR distribution from a narrow, circularly power density spot are presented.

In Fig. (16) the ratio between the S_{ab} and SAR is estimated to be $kx = 0.8$, and $ky = 0.81$ in the horizontal and vertical directions, respectively.

The peak S_{ab} was calculated from Eq. (6) given an input power of 20 W from the RF signal amplifier and the estimated dimensions from Eq. (3). The formula was applied to the estimated dimensions from the measured temperature profile data (in the x- and y-directions) as shown in Fig. (15)-a, and (15)-b. The combination reconstructs the 3D spot as shown in Fig. (14)-a, and (14)-b, for the measured and fitted data, respectively.

The S_{ab} formula is expressed as follows,

$$S_{ab} = P_{in} \cdot \sqrt{A \times B}, \tag{6}$$

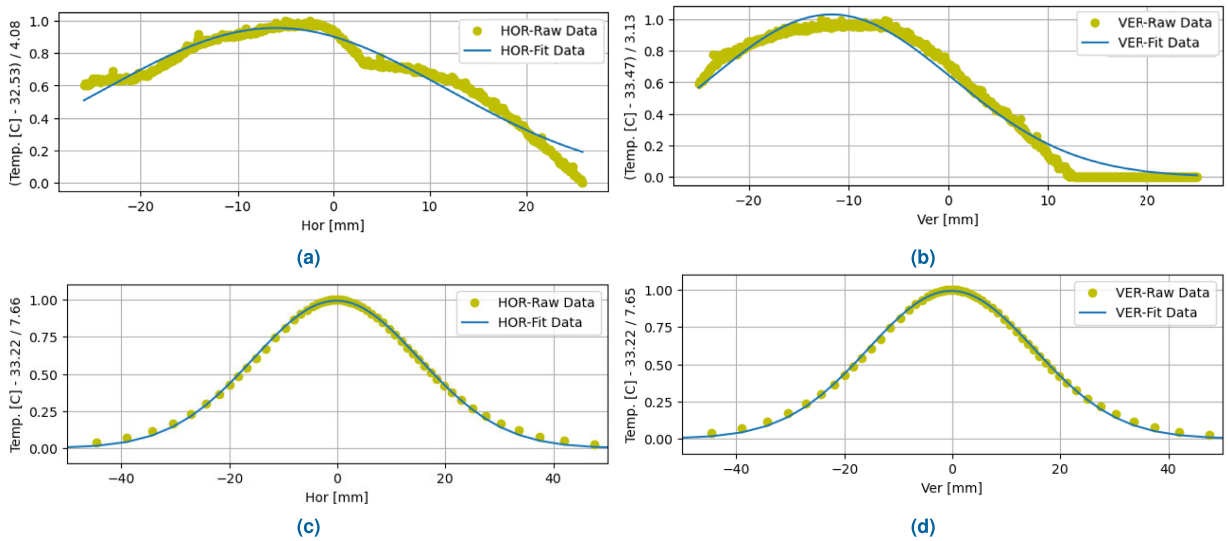

FIGURE 15. 2D temperature data in the horizontal and vertical directions. (a) and (b): measured, (c) and (d): simulated, after 6 min RF exposure.

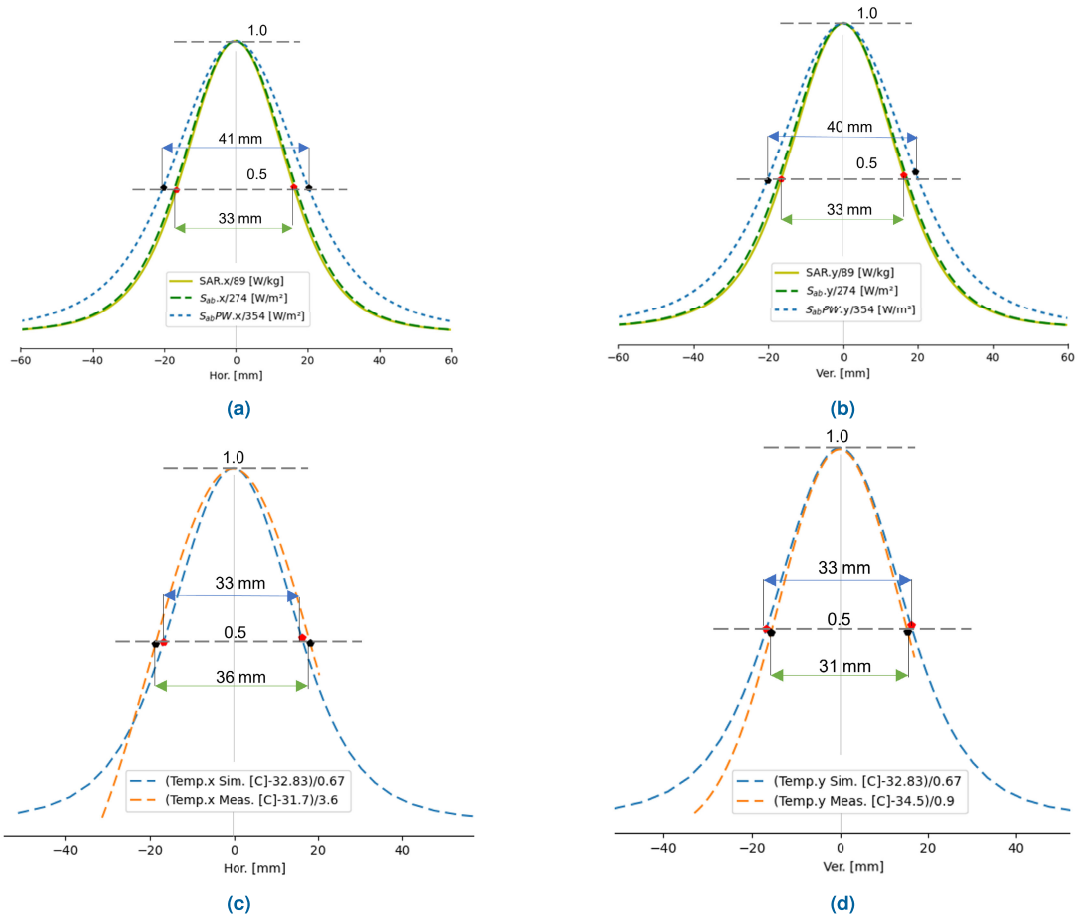

FIGURE 16. The 2D data representation of the SAR, projected power density measured on the skin (S_{ab}), and an unperturbed free-space plane wave power density ($S_{ab}PW$) measured at 50 mm from the waveguide aperture, (a) horizontal & (b) vertical lines at maximum temperature. A comparison between the simulated and measured temperature profiles is made for (c) horizontal and (d) vertical lines. The temperature profiles are captured after 40 seconds of RF exposure. The plots show a normalized peak of each line.

where P_{in} is the RF input power, A and B are constants describing the normalized spot size in the horizontal and vertical dimensions, respectively. For the present example, the S_{ab} and SAR data were estimated as shown in Table (2). As shown in Fig. (17), the RF-EMF thermal response is captured after 6-min exposure with a maximum temperature

TABLE 2. Measured 3D Temperature (40 seconds RF exposure) and SAR profiles data.

		Temp. Profile	SAR Profile
FWHM x-Hor	$[mm]$	36.9	NA
FWHM y-Ver	$[mm]$	31.1	NA
S_{ab}	$[W/m^2]$	150.87	173.54
SAR	$[W/kg]$	85.98	NA

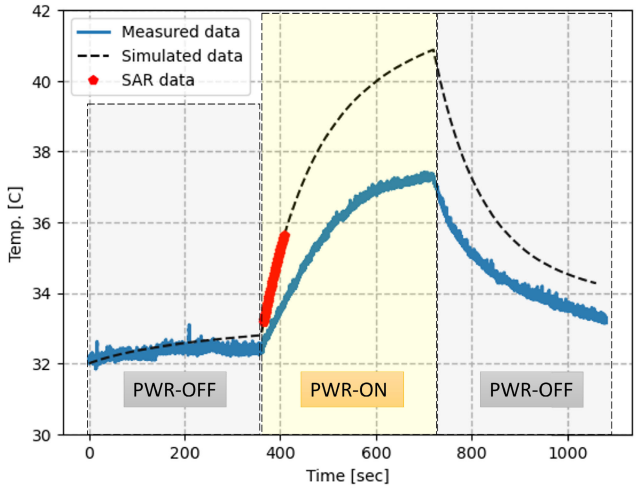

FIGURE 17. Temporal temperature profile using the proposed experimental setup of a human participant. The figure shows a comparison between simulated and measured data for 18 min measurement interval.

of 37.35°C. The measured FWHM was calculated from the line profile data after a brief RF exposure of 40 seconds.

In order to verify the temporal temperature profile results, a thermal simulation in Sim4Life was performed using the thermal transient setup by implementing the three time intervals of the experiment as depicted in Fig. (13) and by comparing it to the measured data. That is, a pre-exposure baseline, RF power-on, and RF power-off intervals are observed as shown in Fig. (17). Overall, a good agreement was achieved during the power-on interval that captured both the initial and peak temperature points at approximately 32°C and 41°C, respectively. The slope of the simulated data and the differentiation of temperature over time were higher compared to the measured data resulting in a difference in estimating the peak SAR when substituting C in Eq. (4). A temperature offset was also observed during the power-off intervals as a result of the observed peak temperature in the measured and simulated data although it shows a similar decaying rate.

Overall, the results of the fabricated and simulated waveguide designs were in close agreement in estimating the 3-layer tissue SAR and power densities. Thus, the measured spot size can also be estimated using the simulation environment when considering an ideal flat surface normal to the waveguide aperture. Further, the simulated design has helped in predicting the spot size for a given waveguide separation distance from the exposed area.

VII. CONCLUSION

In this paper we presented the construction and characterization of a dual port open-ended square waveguide antenna designed to generate a focused 6.1 GHz RF-EMF spot on the skin surface. Computer simulations were used to confirm that the proposed antenna produced the desired spot size and resulting temperature rise on the skin surface. The fabricated waveguide was validated and integrated with other hardware peripherals to comprise the full EM bioheat exposure system. Human pilot testing was conducted to investigate the bio-EM response and the results showed that the system was able to produce the desired local peak temperature rise of ∼37.35°C on the skin surface within 6 min. Overall, we demonstrated the potential of this type of exposure system in heating the skin surface for the proposed bioheat application where the relation between the exposure spot and thermal conduction problem has been verified. Future studies using this system will consider individual differences (e.g. skin tissue thickness, blood flow, age, sex) and environmental factors (e.g. ambient air temperature, humidity) that may influence local skin temperature responses to 6.1 GHz RF-EMF exposures on the forearm and other body regions of interest.

REFERENCES

[1] K. Karipidis, R. Mate, D. Urban, R. Tinker, and A. Wood, "5G mobile networks and health—A state-of-the-science review of the research into low-level RF fields above 6 GHz," *J. Exposure Sci. Environ. Epidemiol.*, vol. 31, no. 4, pp. 585–605, Jul. 2021.

[2] International Commission on Non-Ionizing Radiation Protection (ICNIRP), "Guidelines for limiting exposure to electromagnetic fields (100 kHz to 300 GHz)," *Health Phys.*, vol. 118, no. 5, pp. 483–524, May 2020.

[3] *IEEE Standard for Safety Levels With Respect to Human Exposure to Electric, Magnetic, and Electromagnetic Fields, 0 Hz to 300 GHz*, IEEE Standard C95.1-2019 (Revision of IEEE Std C95.1-2005/Incorporates IEEE Std C95.1-2019/Cor 1-2019), Oct. 2019, pp. 1–312.

[4] V. Anderson, R. Croft, and R. L. McIntosh, "SAR versus S(inc): What is the appropriate RF exposure metric in the range 1–10 GHz, Part I: Using planar body models," *Bioelectromagnetics*, vol. 31, no. 6, pp. 454–466, Sep. 2010.

[5] R. L. McIntosh and V. Anderson, "SAR versus S_{inc}: What is the appropriate RF exposure metric in the range 1–10 GHz? Part II: Using complex human body models," *Bioelectromagnetics*, vol. 31, no. 6, pp. 467–478, 2010.

[6] H. H. Pennes, "Analysis of tissue and arterial blood temperatures in the resting human forearm," *J. Appl. Physiol.*, vol. 1, no. 2, pp. 93–122, Aug. 1948.

[7] A. Hirata, S. Kodera, K. Sasaki, J. Gomez-Tames, I. Laakso, A. Wood, S. Watanabe, and K. R. Foster, "Human exposure to radiofrequency energy above 6 GHz: Review of computational dosimetry studies," *Phys. Med. Biol.*, vol. 66, no. 8, Apr. 2021, Art. no. 08TR01.

[8] K. R. Foster, M. C. Ziskin, Q. Balzano, and A. Hirata, "Thermal analysis of averaging times in radio-frequency exposure limits above 1 GHz," *IEEE Access*, vol. 6, pp. 74536–74546, 2018.

[9] K. R. Foster, M. C. Ziskin, and Q. Balzano, "Thermal response of human skin to microwave energy: A critical review," *Health Phys.*, vol. 111, no. 6, pp. 528–541, 2016.

[10] G. C. van Rhoon, T. Samaras, P. S. Yarmolenko, M. W. Dewhirst, E. Neufeld, and N. Kuster, "CEM43°C thermal dose thresholds: A potential guide for magnetic resonance radiofrequency exposure levels?" *Eur. Radiol.*, vol. 23, no. 8, pp. 2215–2227, Aug. 2013, doi: 10.1007/s00330-013-2825-y.

[11] K. R. Foster, M. C. Ziskin, and Q. Balzano, "Time-temperature thresholds and safety factors for thermal hazards from radiofrequency energy above 6 GHz," *Health Phys.*, vol. 121, no. 3, pp. 234–247, 2021.
[12] *Ansys HFSS*, Ansys, Canonsburg, PA, USA, 2021.
[13] A. Taflove, S. C. Hagness, and M. Piket-May, "Computational electromagnetics: The finite-difference time-domain method," in *The Electrical Engineering Handbook*, vol. 3. Amsterdam, The Netherlands: Elsevier, 2005, p. 629–670, doi: 10.1016/B978-012170960-0/50046-3.
[14] G. B. Gajda, E. Lemay, and J. Paradis, "Model of steady-state temperature rise in multilayer tissues due to narrow-beam millimeter-wave radiofrequency field exposure," *Health Phys.*, vol. 117, no. 3, pp. 254–266, 2019.
[15] M. C. Decreton and F. E. Gardiol, "Simple nondestructive method for the measurement of complex permittivity," *IEEE Trans. Instrum. Meas.*, vol. IM-23, no. 4, pp. 434–438, Dec. 1974.
[16] M. C. Decreton and V. Andriamiharisoa, "Non-destructive measurement of complex permittivity for dielectric slabs," in *Proc. 4th Eur. Microw. Conf.*, Oct. 1974, pp. 71–75.
[17] K. S. Nikita and N. K. Uzunoglu, "Analysis of the power coupling from a waveguide hyperthermia applicator into a three-layered tissue model," *IEEE Trans. Microw. Theory Techn.*, vol. 37, no. 11, pp. 1794–1801, 1989.
[18] L. Lewin, *Advanced Theory of Waveguides* (Associated Iliffe Technical Books). London, U.K.: Iliffe & Sons, Limited, 1951. [Online]. Available: https://books.google.ca/books?id=nPRUAAAAMAAJ
[19] N. Kuster, V. Santomaa, and A. Drossos, "The dependence of electromagnetic energy absorption upon human head tissue composition in the frequency range of 300–3000 MHz," *IEEE Trans. Microw. Theory Techn.*, vol. 48, no. 11, pp. 1988–1995, 2000.
[20] S. I. Alekseev and M. C. Ziskin, "Local heating of human skin by millimeter waves: A kinetics study," *Bioelectromagnetics*, vol. 24, no. 8, pp. 571–581, Dec. 2003.
[21] T. Nakae, D. Funahashi, J. Higashiyama, T. Onishi, and A. Hirata, "Skin temperature elevation for incident power densities from dipole arrays at 28 GHz," *IEEE Access*, vol. 8, pp. 26863–26871, 2020.
[22] *2500B Series Microwave Signal Generators*, Giga-Tronics, Dublin, CA, USA, Dec. 2014.
[23] Microwaveamps. *Product: AM43-5.8-6.4-47-47*. Accessed: Jun. 2023. [Online]. Available: https://microwaveamps.co.uk/RF-amplifier/product/5939
[24] *R& S NRP-Zxx Power Sensors Specifications*, Rohde & Schwarz, Munich, Germany, Apr. 2019.
[25] *FLIR A400/A500/A700 series*, FLIR, OR, USA, Jun. 2022.
[26] P. A. Hasgall, F. Di Gennaro, C. Baumgartner, E. Neufeld, B. Lloyd, M. C. Gosselin, D. Payne, A. Klingenböck, and N. Kuster, "IT'IS database for thermal and electromagnetic parameters of biological tissues," Version 4.1, Feb. 2022, doi: 10.13099/VIP21000-04-1.

ABDELELAH ALZAHED (Member, IEEE) received the B.Sc. and M.Sc. degrees from the Communication and Electronics Engineering Department, Arab Academy for Science, Technology and Maritime Transport (AASTMT), Cairo, Egypt, in 2008 and 2014, respectively, and the Ph.D. degree in antenna theory and machine learning applications from the Electrical and Computer Engineering Department, Royal Military College of Canada (RMC), Kingston, ON, Canada, in 2019. His field of study involved inverse source problems (ISPs), singularity expansion method (SEM), and machine learning. In 2020, he joined the Consumer and Clinical Radiation Protection Bureau, Non-Ionizing Radiation Physical Sciences Division, Health Canada, as a Senior Radio Frequency Engineer. His research interests include electromagnetic theory, radiofrequency testing techniques, numerical modeling, and data processing and machine learning solutions in electromagnetics. He has also collaborated actively with researchers in several other disciplines of biomedical sciences and technology.

ERIC LEMAY received the Diploma degree in electronics engineering technology from La Cité collégiale, in 1997. He was employed as a Technical Inspector with the Consumer and Clinical Radiation Protection Bureau (Non-Ionizing Radiation Physical Sciences Division), Health Canada, from 1999 to 2022. There, he worked on the design and implementation of RF measurement instrumentation, performed laboratory experiments, and worked on RF exposure modeling in support of safety code 6. He is currently employed by the Communications Research Centre, Government of Canada.

MYKOLA ZHUK received the Diploma degree (Hons.) in radiophysics and electronics and the Cand.Phys.Math.Sci. and Dr.Phys.Math.Sci. degrees in radiophysics from Gorky Kharkiv State University, Ukraine, in 1978, 1982, and 1991, respectively. From 1981 to 1997, he served as a Junior and Senior Researcher, a Senior Lecturer, and a Professor with the Department of Theoretical Radiophysics, Gorky Kharkiv State University. Subsequently, from 1998 to 2018, he worked as a Filter Design Engineer at Unique Broadband Systems Ltd., Ottawa, ON, Canada. Since 2019, he has been serving as an RF Radiation Specialist with the Consumer and Clinical Radiation Protection Bureau, Health Canada, Ottawa. From 1993 to 1995, he was a Research Fellow of the Alexander von Humboldt Foundation, Institute for Microwave Engineering, Technical University of Hamburg-Harburg, Hamburg, Germany. He has advised three Cand.Sci. students and served as a scientific consultant to three researchers pursuing a Dr.Sci. degree. He has authored or coauthored over 60 articles in leading international journals. His research interests include wave propagation in random and complex media (1978–1997), CAD of passive microwave components (1998–2018), and EM wave interaction with the human body (since 2019). He is a member of the Electromagnetics Academy, MA, USA.

GREGORY B. GAJDA received the master's degree in electrical engineering from the University of Ottawa, Ottawa, ON, Canada, in 1982. From 1981 to 1987, he was a Research and Development Engineer in microwave and millimeter-wave active and passive circuits and subsystems for the Canadian Government. From 1987 to 1993, he was employed as a Microwave Component Design Engineer in the private sector. Since 1993, he has been a Scientist with the Consumer and Clinical Radiation Protection Bureau (Non-Ionizing Radiation Physical Sciences Division), Health Canada. He is the coauthor of *Health Canada's Safety Code 6* (recommended human exposure limits for radiofrequency fields in the 100 kHz to 300 GHz frequency range) and has coauthored peer-reviewed publications in the areas of dielectric measurement, in-vivo and in-vitro exposure system designs and nerve-stimulation, and thermal effects of electromagnetic exposure. He also is a co-holder of a patent for a millimeter-wave amplifier. His research interests include electromagnetic exposure assessment, exposure system design, electromagnetic dosimetry, and thermal effects.

JAMES P. MCNAMEE received the Ph.D. degree in pharmacology and toxicology from the Faculty of Health Sciences, Queen's University, Kingston, ON, Canada, in 1996. Since 1996, he has been employed as a Research Scientist with the Consumer and Clinical Radiation Protection Bureau (Non-Ionizing Radiation Health Sciences Division), Health Canada, and has been an Adjunct Professor with the Department of Biomedical Sciences, Queen's University, since 2001. He was a member of the International Agency for Research on Cancer (IARC) Expert Working Group evaluating the carcinogenicity of radiofrequency fields, is a member of the World Health Organization (WHO) EMF Project—International Advisory Committee and the coauthor of *Health Canada's Safety Code 6* (recommended human exposure limits for radiofrequency fields in the 100 kHz to 300 GHz frequency range). He has authored or coauthored over 100 peer-reviewed scientific articles. His research interests include gene expression, genotoxicity, and signal transduction changes in response to radiofrequency and optical radiation exposures in animals and human-derived cell lines.

GREGORY W. MCGARR (Member, IEEE) received the Ph.D. degree in environmental ergonomics from the Faculty of Applied Health Sciences, Brock University, St. Catharines, ON, Canada, in 2017. From 2017 to 2020, he was a Postdoctoral Research Fellow with the Human and Environmental Physiology Research Unit, School of Human Kinetics, University of Ottawa, Ottawa, ON, Canada. He is currently a Research Scientist with the Consumer and Clinical Radiation Protection Bureau (Non-Ionizing Radiation Health Sciences Division), Health Canada, and an Adjunct Professor with the School of Human Kinetics, University of Ottawa. He is also currently a member of the WHO Task Group in radiofrequency fields and health. His research interests include human thermoregulation, including the physiology and pharmacology of skin blood flow and sweating, responses to heat exposure and potential countermeasures in vulnerable populations, as well as temperature-related effects of radiofrequency field exposures in humans and human-derived cell lines.